Soft Matter

PAPER

View Article Online
View Journal | View Issue

Open Access Article. Published on 31 August 2022. Downloaded on 10/18/2025 7:44:19 PM.
This article is licensed under a Creative Commons Attribution-NonCommercial 3.0 Unported Licence.

Check for updates

Cite this: *Soft Matter*, 2022, **18**, 6848

Producing shape-engineered alginate particles using viscoplastic fluids†

Sima Asadi,[a] Arif Z. Nelson ‡[b] and Patrick S. Doyle *[abc]

Received 12th May 2022,
Accepted 9th August 2022

DOI: 10.1039/d2sm00621a

rsc.li/soft-matter-journal

Non-spherical hydrogel particles are of fundamental interest and can find use in a variety of applications ranging from pharmaceuticals to biomedical to food. Here, we report a new method that leverages the yield stress property of viscoplastic fluids to synthesize shape-engineered alginate particles. By dripping an aqueous viscoplastic solution composed of sodium alginate and a yield-stress material into an ionic gelation bath, droplets are controllably deformed and crosslinked, producing a wide assortment of shapes. We find that by tuning the yield stress of the solution and the nozzle tip orientation, a range of shapes from symmetric and near-spherical, to asymmetric and anisotropic (*e.g.*, egg-, rice grain-, arc-, ring-, snail shell-, tear-, and tadpole-like) can be produced. We explain our observations using scaling analysis of the forces exerted on the droplet at different stages of particle production. We show that the main factors that determine the degree of droplet deformation during bath entry and the final appearance of the alginate particles are the initial shape of the droplets, the timescales of the viscoplastic fluid relaxation *versus* the crosslinking reaction, and the physico-chemical properties of the yield-stress material.

1 Introduction

Hydrogel particles are hydrated 3D networks of crosslinked polymer chains that have found diverse application in the biomedical, pharmaceutical, environmental, food, and cosmetic industries due to their versatile nature with highly tunable physical and chemical properties.[1–5] Hydrogel particles are extensively used for controlled drug delivery,[6–8] cell and islet encapsulation,[9–12] scaffold building and 3D biofabrication,[13,14] biosensing,[15] bioactive delivery in aquaculture,[16] and water treatment.[17] Hydrogels can be made of both natural and synthetic polymers.[1] Alginate is a natural anionic polysaccharide derived from brown algae that can be crosslinked in the presence of divalent cations such as Ca^{2+} to form stable hydrogels.[18] Due to its biocompatibility, biodegradability, non-toxicity, low-cost, tunable mechanical properties, and swelling behavior, alginate is an ideal candidate for a wide range of biomedical and pharmaceutical applications.[18,19]

Prior research on producing alginate hydrogel particles has mostly focused on producing spherical shapes. Extrusion is a well-known method used to produce large (>1 mm) spherical alginate particles at a low production rate by simply dripping an alginate solution from a nozzle into a gelation bath.[20–22] This technique can be modified to produce smaller particles at a higher production rate using electrostatic potential,[23,24] a vibrating nozzle,[25] jet-cutting,[26] and centrifugal force.[27,28] Emulsification methods such as mechanical stirring and high-speed homogenization that involve dispersing an alginate solution in an immiscible liquid followed by a gelation process are also used to produce a broad range of particles from 10 to 1000 μm.[21,29] Over the past two decades, there has been a growing interest in microfluidics to produce spherical alginate particles because it allows for precise control over size, production rate, and properties of the particles.[30–33]

Non-spherical hydrogel particles have received tremendous attention in the past decade because of several advantageous features they offer compared to the more common spherical particles. These features include higher surface area-to-volume ratios, shorter diffusion distances for encapsulated loads,[10,34] anisotropic responses to external stimuli,[35,36] better attachment to cells and tissues,[37,38] enhanced targeting as drug carriers, and controllable drug circulation and release dynamics inside the body.[39,40] Given these advantages, numerous methods have been developed to produce non-spherical hydrogel particles from different polymer systems (see Cai *et al.*,[41] Zhu *et al.*,[42] Dendukuri *et al.*,[30] Champion *et al.*,[37]

[a] *Department of Chemical Engineering, Massachusetts Institute of Technology, Cambridge, MA 02139, USA. E-mail: pdoyle@mit.edu*
[b] *Critical Analytics for Manufacturing Personalized-Medicine, Singapore-MIT Alliance for Research and Technology, Singapore 138602, Singapore*
[c] *Harvard Medical School Initiative for RNA Medicine, Boston, MA 02215, USA*

† Electronic supplementary information (ESI) available. See DOI: https://doi.org/10.1039/d2sm00621a

‡ Present address: Food, Chemical and Biotechnology Cluster, Singapore Institute of Technology, Singapore 138683, Singapore.

This journal is © The Royal Society of Chemistry 2022

Open Access Article. Published on 31 August 2022. Downloaded on 10/18/2025 7:44:19 PM.
This article is licensed under a Creative Commons Attribution-NonCommercial 3.0 Unported Licence.

and the references therein). Less attention, however, has been devoted to produce non-spherical alginate particles and the diversity of the shapes generated with current techniques is limited.

Extrusion dripping combined with microfluidics or electrospraying has been used to produce non-spherical alginate particles (*e.g.*, mushroom-like, hemispherical, red blood cell-like, and tadpole-like shapes) by altering parameters such as the distance between nozzle tip and gelation bath surface, fluid (extruded fluid or bath) viscosity, and surface tension.[36,40,43–45] Anisotropic gelation of an alginate solution extruded from a bevel-tip capillary was also used to produce hydrogel microsprings.[46] Recently, 'vortex ring freezing' method has been developed and used to produce toroidal alginate and chitosan particles. In this technique, the droplets from an electrospray nozzle enter a miscible fluid bath during which they deform and experience various intermediate shapes. These intermediate shapes can be frozen into particles in order to make teardrop, jelly fish, and toroidal shapes.[34,47]

In this work, we report a new method to produce non-spherical alginate particles by making use of viscoplastic fluids. Viscoplastic fluids (also known as yield-stress fluids) are a class of complex materials that behave like an elastic solid below a threshold applied stress (*i.e.* a 'yield stress'), and flow like a fluid above the yield stress.[48–50] Viscoplastic materials are abundant among everyday cosmetic and food products (*e.g.*, toothpaste and ketchup). Due to their extremely useful flow behaviour, there is a growing interest in these materials for various applications including drug delivery[51] and 3D printing of continuous structures.[52,53] Recently, a new technique has been developed for 'embedded droplet printing' in which individual droplets are generated and fixed in place inside a yield-stress fluid bath that can subsequently be manipulated and used for biological assays and as microreactors.[54,55] Dripping behavior of viscoplastic fluids has also been extensively investigated. It has been shown that the drops of viscoplastic fluids formed at the nozzle tip, transition from spherical to prolate shapes by increasing the yield stress value.[56–59] Here, we leverage the ability of viscoplastic fluids in forming non-spherical droplets and combine it with the gel-forming capacity of sodium alginate to tune the shape of alginate particles. We use the extrusion dripping technique to drip non-spherical viscoplastic droplets composed of sodium alginate and a yield-stress material into a $CaCl_2$ gelation bath. We use two yield-stress materials with distinct microstructures for which the yield stress comes about by either jammed, repulsive or networked, attractive, interactions. We show that after vertical bath entry of the prolate viscoplastic droplets, they undergo further deformation and a crosslinking reaction, producing a range of shapes from near-spherical to egg-, rice grain-, and tear-like. In addition, we find that tuning the nozzle orientation alters the shape of viscoplastic droplets significantly and intensifies the degree of droplet deformation during bath entry, yielding an assortment of spectacular asymmetric, anisotropic, shapes. We further demonstrate that changing the type of yield-stress material can affect the shape, size, and appearance of the alginate particles. We find that within our investigated range, increasing the concentration of the gelation bath did not have a significant effect on the shape and size of the particles.

2 Materials and methods

2.1 Preparing solutions

Materials. Carbomer 940 (polyvinyl carboxy polymer cross-linked with ethers of pentaerythritol to form polyacrylic acid) was obtained from MakingCosmetics. Xanthan gum (G1253), sodium alginate (W201502), sodium hydroxide (71690), and calcium chloride (C1016) were purchased from Sigma-Aldrich.

Viscoplastic solution preparation. We prepared nine aqueous viscoplastic solutions containing sodium alginate and either Carbomer (C) or xanthan gum (X) which are additives known to produce a yield-stress fluid at sufficient concentrations; Carbomer 940 forms a jammed microgel solution and xanthan gum forms a gel network. Five sodium alginate-Carbomer solutions were prepared by mixing 0.5 wt% sodium alginate with different concentrations of Carbomer in DI water (hereafter denoted as C-σ_y, where σ_y is the yield stress of the solution). Carbomer powder was mixed with DI water for 30 min at 1000 rpm and room temperature. Sodium alginate powder was then added to the solution and stirring was continued for an additional 30 min at 1600 rpm. The solutions were neutralized to pH of 6.5–7 by adding a 1 M NaOH solution. Four sodium alginate-xanthan gum solutions were also prepared by mixing 0.5 wt% sodium alginate with xanthan gum in DI water (hereafter denoted as X-σ_y, where σ_y is the yield stress of the solution). Xanthan gum powder was slowly added to DI water while being mixed with an overhead stirrer at 700 rpm and room temperature for 5 minutes. Then the solution was placed on a hot plate at 80 °C and mixed at 400 rpm for an additional 30 min. Sodium alginate powder was then added to the solution and stirring was continued for 30 min at 1600 rpm with the heating element turned off. Before performing the experiments, a few drops of food dye (blue for C-σ_y and green for X-σ_y solutions) were added to all nine solutions in order to increase their visibility during imaging. Solutions were centrifuged at 2000 rpm for 15 min to remove air bubbles.

Gelation bath preparation. Three $CaCl_2$ aqueous solutions were prepared by mixing 2, 10, and 20 wt% $CaCl_2$ granular powder with DI water. 0.1 wt% Tween 80 was added to lower the surface tension.

2.2 Rheological characterization

Rheological measurements were performed using a TA Instruments DHR-3 combined motor/transducer rotational rheometer with a flat-plate upper geometry (diameter = 40 mm) and bottom Peltier plate at 25 °C; results are shown in Fig. 1(a) and (b). Sand paper (Norton, grit = 180) was used to avoid slip at low shear rates. Shear-rate controlled experiments were performed in the shear rate range of $10^{-2} < \dot{\gamma} < 10^{2}$ and $10^{-2} < \dot{\gamma} < 1$ for C-σ_y and X-σ_y solutions, respectively. Note that xanthan gum formulations are generally thixotropic and we only

Open Access Article. Published on 31 August 2022. Downloaded on 10/18/2025 7:44:19 PM.
This article is licensed under a Creative Commons Attribution-NonCommercial 3.0 Unported Licence.

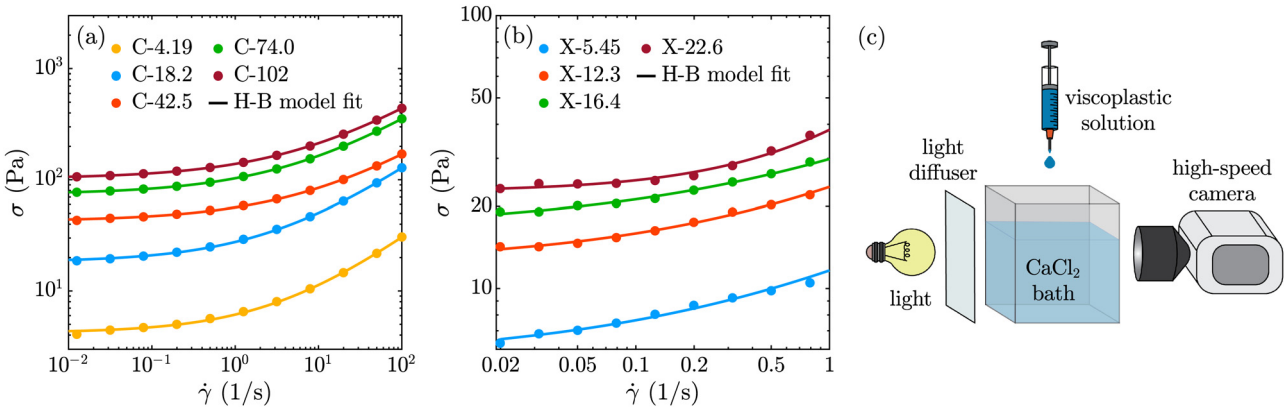

Fig. 1 Shear-rate controlled test results for (a) C-σ_y and (b) X-σ_y solutions. The solid curves correspond to Herschel Bulkley (H–B) model fits used to calculate the yield stress of the solutions, σ_y. (c) Experimental setup to study viscoplastic droplet formation at the nozzle tip, its entry to a $CaCl_2$ bath, and its deformation and ionic crosslinking to form alginate particles.

observed a clear yield-stress signature for X-σ_y solutions when ramping the shear rate from low to high. Carbomer solutions, on the other hand, are non-thixotropic and for our C-σ_y solutions, the yield stress measurements were independent of the ramp direction. For consistency, we present low-to-high shear rate ramp data for both formulations, and therefore probe the static yield stress. The data sets were fit to the Herschel–Bulkley model to obtain the shear yield stress of the samples ($\sigma = \sigma_y + k\dot{\gamma}^n$, where σ, σ_y, k, and n are shear stress, yield stress, consistency index, and flow index, respectively).

2.3 Experiments

Fig. 1(c) shows a schematic of the experimental setup used to produce shape-engineered alginate particles. Viscoplastic solutions (C-σ_y and X-σ_y) were dripped from a 14G nozzle (Nordson EFD, inner diameter D_0 = 1.54 mm, length = 12.7 mm) into a $CaCl_2$ gelation bath using a syringe pump (Harvard Apparatus, PHD 2000 series, Infuse/Withdraw) operating at Q_0 = 0.05 ml min^{-1}. For selecting a value for Q_0, we ensured that a small variation in the flow rate does not alter the shape of extruded filaments and droplets. The nozzle was positioned at an angle θ with respect to the horizontal direction (*i.e.*, $\theta = 90°$ for a vertical nozzle). The distance between the nozzle tip and bath surface was $h \approx 4$ cm and the droplet impact velocity, U_0, was measured using image processing just before the droplet impacts the bath surface. Previous work measuring the surface tension of Carbopol and xanthan gum solutions found only small deviations from that of water, and therefore, here we use the surface tension of water (*i.e.*, γ = 0.072 N m^{-1} at 20 °C) for our calculations.[60,61] A Phantom Miro M 320S Vision Research high-speed camera connected to a Nikon AF-S DX Nikkor 18–70 mm lens recorded the process at a resolution of 1024 × 1024 pixels. Droplet formation and pinch-off at the nozzle tip were recorded at 200 fps, while the droplet free fall in the air and bath entry were recorded at 2000 fps. After the bath entry, droplets were allowed to stay in the gelation bath until the crosslinking reaction was complete and the food dye diffused out completely. The resultant alginate particles were then removed from the bath and washed with DI water several times. We then allowed the particles to stay in DI water for 48 h before taking their images to ensure that they were in an equilibrium swollen state. Finally, images of the particles were captured with an LCD digital microscope (PalliPartners, ASIN B08LVM9361) while they were inside the DI water. Different approaches may be used to calculate the size of droplets and particles using either their volume or projected area (Fig. S1, ESI†). Considering the asymmetric shape of the droplets and particles in our experiments, calculating an accurate volume is a challenging task. Therefore, for consistency in our analysis, we chose to use 2D images of the droplets and particles to calculate their projected area diameter, *i.e.*, $D_A = (4A/\pi)^{1/2}$.

3 Results and discussion

3.1 Effect of σ_y

Fig. 2 shows the stages of producing alginate particles from C-σ_y solutions dripped from a 14G nozzle angled at $\theta = 90°$ into a 2 wt% $CaCl_2$ gelation bath. During the droplet formation stage, a competition between surface tension and yield-stress forces, described with the dimensionless number $\beta = \sigma_y D_A/\gamma$, determines the initial shape of the droplets.[57] At low σ_y ($\beta \sim O(0.1)$), surface tension force deforms the fluid filament that is extruded from the nozzle to a pear-like shape (Fig. 2(a), column 1). As σ_y increases ($\beta \sim O(1\text{–}10)$), the filament is less deformed and it takes a more prolate shape (Fig. 2(b)–(e), column 1). In all cases, the filament continues growing until the normal stress due to the fluid weight ($\sim \rho_f g L$), exceeds its elongational yield-stress, $\sigma_{y,e}$ ($\approx \sqrt{3}\sigma_y$).[62] At a critical filament length of $l_c \sim \sigma_{y,e}/(\rho_f g)$ the fluid yields locally below the nozzle tip and necking starts. At this stage, neck diameter, D_n, continues decreasing as the normal stress increases with $\sim 1/D_n^2$,[56,59] and eventually the droplet pinches off (Fig. 2(b)–(e), column 2). After the onset of necking until the droplet pinches off, its length, L, does not change significantly and can be approximated by l_c (Fig. 3). Upon pinch-off the rear end of droplet and the residual fluid tip attached to the nozzle slightly retract. During the free fall

 This journal is © The Royal Society of Chemistry 2022

Open Access Article. Published on 31 August 2022. Downloaded on 10/18/2025 7:44:19 PM.
This article is licensed under a Creative Commons Attribution-NonCommercial 3.0 Unported Licence.

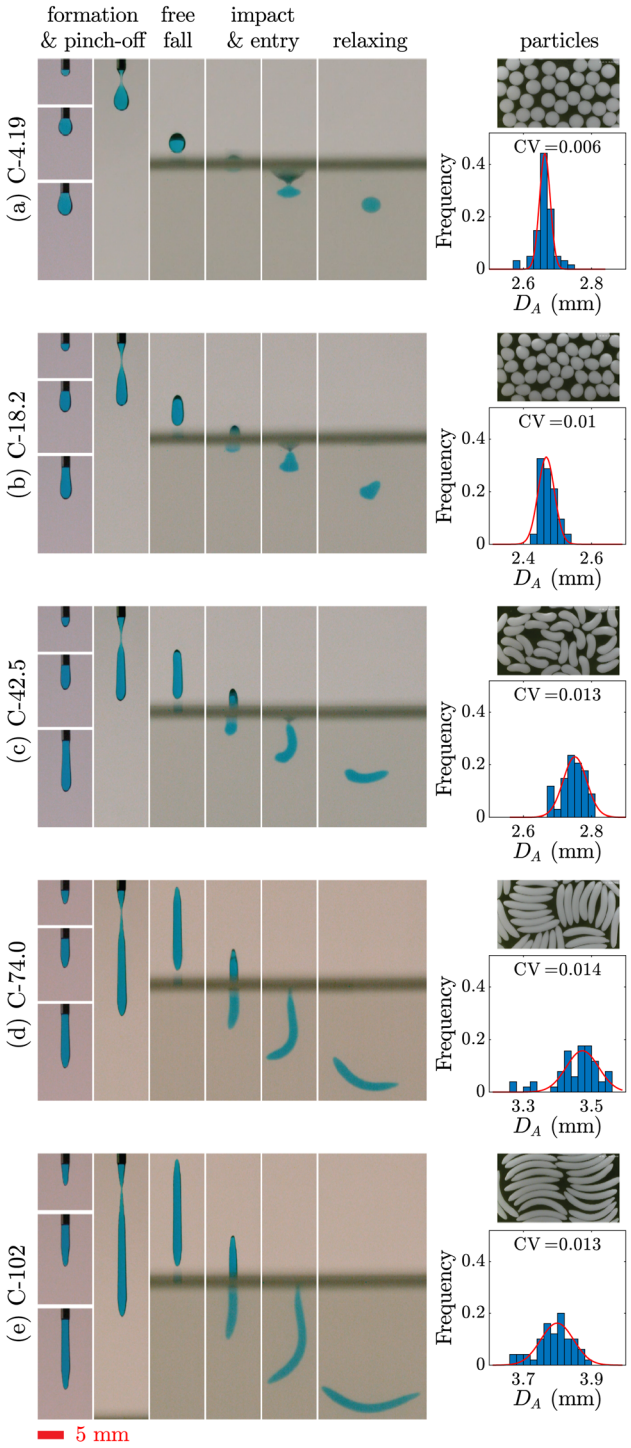

Fig. 2 Effect of σ_y on the shape of alginate particles. Particles are formed by dripping (a) C-4.19, (b) C-18.2, (c) C-42.5, (d) C-74.0, and (e) C-102 solutions from a 14G vertical nozzle (θ = 90°) into a 2 wt% $CaCl_2$ bath. The columns show different stages of the particle production, final shape of the particles, and histograms of the projected area diameter, D_A, for the particles. The red scale bar is 5 mm for all images and the corresponding videos are provided in Movie S1 (ESI†).

(Fig. 2(b)–(e), column 3), all droplets maintain their shape since the drag force in the air ($\sim \rho_a C_D U_0^2 D_A^2$) is not strong enough to overcome the yield stress ($\sim \sigma_y D_A^2$) and deform the droplets.[63]

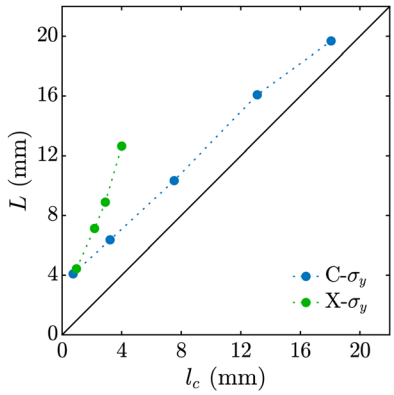

Fig. 3 Droplet length, L, *versus* critical length, $l_c = \sigma_{y,e}/(\rho_f g)$, for C-$\sigma_y$ and X-σ_y solutions. Each data point is the average of 3 trials and the error bars (not shown) are smaller than the marker size. Dotted lines are used as a guide for the eyes.

When C-4.19 and C-18.2 droplets impact the bath surface with $U_0 = 0.81 \pm 0.01$ m s^{-1}, the bottom of the droplets flattens and they take oblate and pear-like shapes, respectively (Fig. 2(a) and (b), columns 4 and 5). Previous work on water entry of viscoplastic Carbopol droplets showed more deformation at this range of σ_y and U_0 than observed here.[63] The smaller deformation observed in our experiments can be attributed to the presence of sodium alginate in our viscoplastic solutions and the ionic crosslinking reaction that begins upon droplet entry to the gelation bath. For C-42.5, C-74.0, and C-102 solutions, the droplet tip deformation upon impact ($U_0 = 0.69 \pm 0.05$ m s^{-1}) is less pronounced due to higher σ_y (Fig. 2(c)–(e), column 4). The small difference observed between the impact velocities of the droplets despite having similar release heights ($h \approx 4$ cm), is due to the difference in the length of the droplets. Upon impact, the droplet is perturbed and an overturning couple is formed that makes the droplet tip move in the lateral direction and rotate as it penetrates into the bath.[64] While the lower part of the droplet decelerates due to impact and higher drag force exerted by the bath ($\sim \rho_b C_D U_0^2 D_A^2$), its upper part falls almost freely, leading to a vertical velocity mismatch. Therefore, the droplet buckles elastoplastically during the bath entry (Fig. 2(c)–(e), column 5).

After the rear end of the deformed viscoplastic droplet detaches from the bath surface, it relaxes partially during sinking (Fig. 2(a)–(e), column 6). At this stage, a competition between the time scales of the viscoplastic fluid relaxation and the crosslinking reaction plays an important role in determining the final shape of the particles. Although, the time required for full crosslinking might be higher than the relaxation time scale,[65–67] a partial crosslinking that starts from the edges of droplet might be strong enough to limit the degree of relaxation and freeze the shape of particle. The final shape of the particles are depicted in the last column of Fig. 2(a)–(e) along with the histograms of their projected area diameter. A range of shaped particles from near-spherical to egg-like and rice grain-like were produced. The small coefficient of variation (CV = SD/μ) of the particle size distributions indicate that the particles were

Open Access Article. Published on 31 August 2022. Downloaded on 10/18/2025 7:44:19 PM.
This article is licensed under a Creative Commons Attribution-NonCommercial 3.0 Unported Licence.

uniform in size. The images of Fig. 2 show that the sizes of particles are smaller than the sizes of uncrosslinked droplets, even in their fully swollen (un-dried) state. It is unlikely that this shrinkage is due to diffusion of the Carbomer macromolecules out of the particles into the bath considering the diffusion time scale of Carbomer ($O(10^3$–$10^4)$ s),[68] and the fact that the particles shrink considerably during the first few minutes of bath entry. In addition, comparing the alginate mesh size ($\approx$ 10–100 nm depending on the polymer solution and gelation bath concentration[69]) and the size of unswollen Carbomer macromolecules (average diameter $\approx$ 20–410 nm depending on the molecular weight[70]) suggests that Carbomer diffusion is unlikely to happen. Instead, the decrease in the size of particles can be attributed to shrinkage of alginate after gelation.[20] Furthermore, it is known that Carbomer microgels deswell and precipitate in the presence of di- and multi-valent ions.[54,71,72] Therefore, Ca^{2+} ion diffusion from the gelation bath into the particles can contribute to their shrinkage by deswelling the Carbomer.

3.2 Effect of θ

Fig. 4 demonstrates the stages of alginate particle production using C-74.0 and C-102 solutions dripped from a 14G nozzle angled at $\theta = 60°$, $\theta = 30°$, or $\theta = 0°$ into a 2 wt% $CaCl_2$ bath. As mentioned earlier for the case of $\theta = 90°$, the residual fluid attached to the nozzle tip retracts and becomes unyielded quickly after a droplet pinches off. For a tilted nozzle, when fresh fluid is extruded out, the filament initially follows a trajectory in the direction of nozzle tip. However, it quickly yields locally, bends downward, and rotates underneath the nozzle above a critical length of $\sim \sqrt{\sigma_y D_0/(\rho_f g \cos(\theta))}$ due to the action of a gravitational moment which overcomes the yield stress.[73] Note that the filament tip remains unyielded. After the filament collapses toward the vertical direction, it continues growing until its weight exceeds $\sigma_{y,e}$ and the droplet pinches off. After pinch-off, and during the free fall, the droplet buckles plastically with a degree inversely proportional to θ, due to its asymmetric geometry. For C-74.0 solution dripping at $\theta = 0°$, the droplet formation stage differs slightly from other configurations (Fig. 4(c), column 1); as soon as the fluid is extruded out from the nozzle and starts rotating underneath the extrusion point, the tip of the fluid adheres to the outer wall of the nozzle. The filament first coils up like a snail shell, and then as the fluid weight increases, it detaches from the nozzle wall and pinches off.

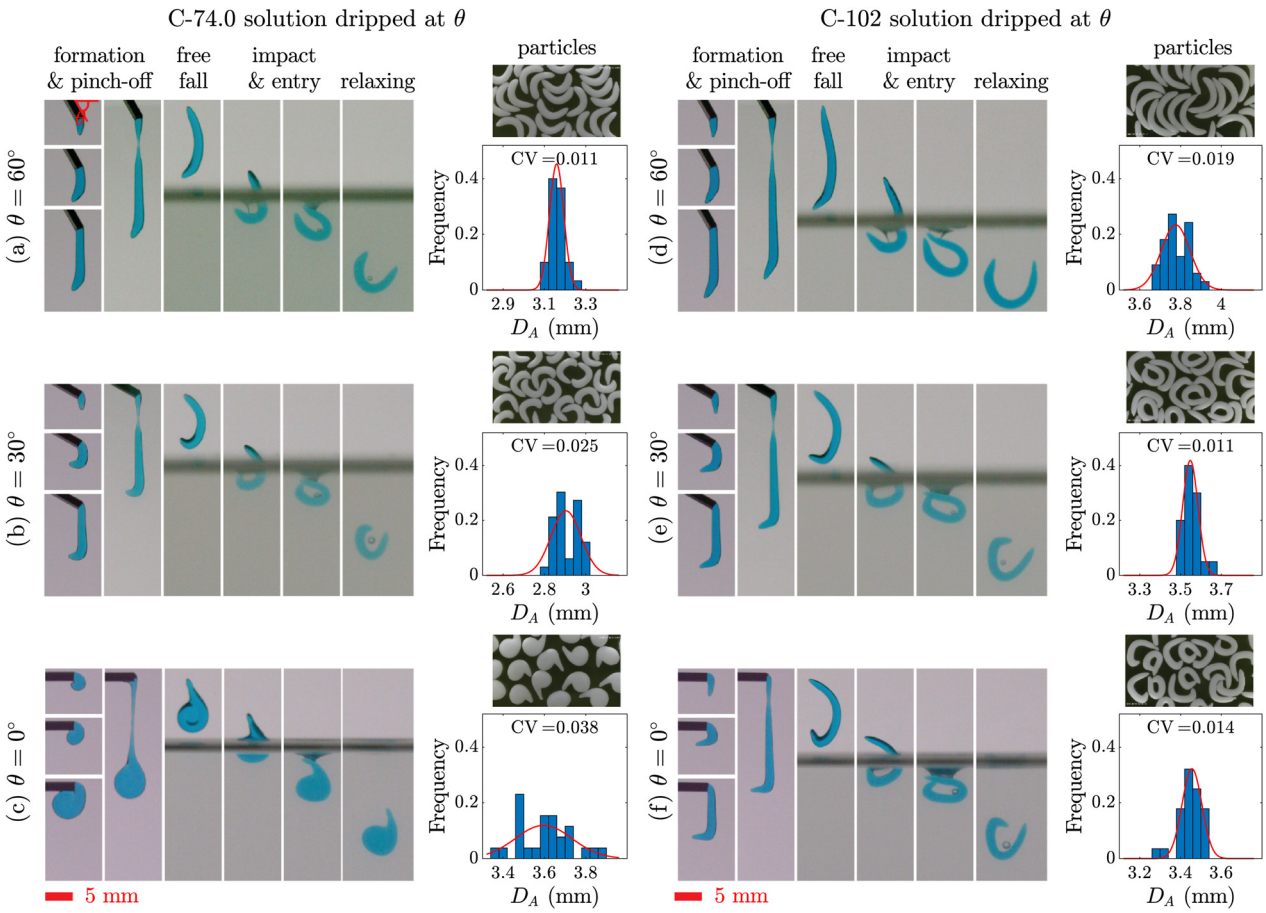

Fig. 4 Effect of θ on the shape of alginate particles. Particles are formed by dripping C-74.0 (left) and C-102 (right) solutions from a 14G nozzle angled at (a), (d) $\theta = 60°$, (b), (e) $\theta = 30°$, or (c), (f) $\theta = 0°$. The columns show different stages of the particle production, final shape of the particles, and histograms of the projected area diameter, D_A, for the particles. The red scale bars are 5 mm for all images and the corresponding videos are provided in Movie S2 (ESI†).

 This journal is © The Royal Society of Chemistry 2022

Open Access Article. Published on 31 August 2022. Downloaded on 10/18/2025 7:44:19 PM.
This article is licensed under a Creative Commons Attribution-NonCommercial 3.0 Unported Licence.

The fundamental mechanism for the droplet impact and entry to the gelation bath for the tilted nozzles is similar to the case of $\theta = 90^\circ$. However, here the droplets have already buckled during the formation and free fall, and therefore are prone to further deformation. When a buckled droplet hits the bath surface, its lower half enters the bath and an air cavity is initially formed. The lower half of the droplet remains attached to the cavity, decelerates significantly, and deforms plastically. The upper half falls with a higher vertical velocity and bends dramatically over the lower half as it falls. When the lower half of the droplet is detached from the cavity, an air bubble sticks to its wall which subsequently detaches from the droplet or bursts. In some configurations (Fig. 4(b), (e), and (f)), the two ends of the droplet come together and form a ring shape. After the droplet pinches off from the bath surface completely, the upper half of the droplet relaxes back slightly and the droplet continues sinking in the bath and fully solidifies. The final shape of the particles and the corresponding size histograms are depicted in the last column of Fig. 4. Snail shell-like and arc-shaped particles were produced by changing θ. Occasionally, for the conditions shown in Fig. 4(e) and (f), the droplet tail sticks to its head during deformation and maintains its shape, forming a ring-shaped particle.

3.3 Effect of changing yield-stress material

To investigate the behavior of an attractive network-based yield-stress fluid and produce a wider range of shaped alginate particles, we replaced Carbomer with a different rheological modifier, xanthan gum. Xanthan gum is a natural polysaccharide produced by *Xanthomonas campestris* bacterium that can be used to prepare shear-thinning[58] and yield-stress fluids.[74] Fig. 5(a) shows the stages of non-spherical alginate particle production using X-σ_y viscoplastic solutions. The formation stage of the X-σ_y droplets (column 1) is very similar to C-σ_y droplets; as σ_y increases, the shape of the droplets becomes more prolate. However, neck length, defined as twice the distance between nozzle tip and minimum neck diameter position, increases significantly before the droplet pinches off (Fig. 5(a), column 2). After pinch-off, X-σ_y droplets are longer than C-σ_y droplets with similar σ_y (Fig. 3). The high extensibility behavior of the X-σ_y solutions can be attributed to the long-chain, stretchy, attractive polymer network of xanthan gum compared to the repulsive-dominated systems with small extensibility such as Carbomer.[75] During the free fall, there is no significant change in the shape of droplets, except the retraction of the neck filament residue upon pinch-off. The X-5.45 droplets flatten upon impact and entry into the 2 wt% $CaCl_2$ bath, producing an oblate shape that subsequently relaxes back partially and generates a particle with an egg-like shape. X-12.3, X-16.4, and X-22.6 droplets buckle as they enter the bath, similar to the C-σ_y droplets. After the droplets completely enter the bath and detach from the bath surface, they partially relax back towards their initial shape and continue sinking until the

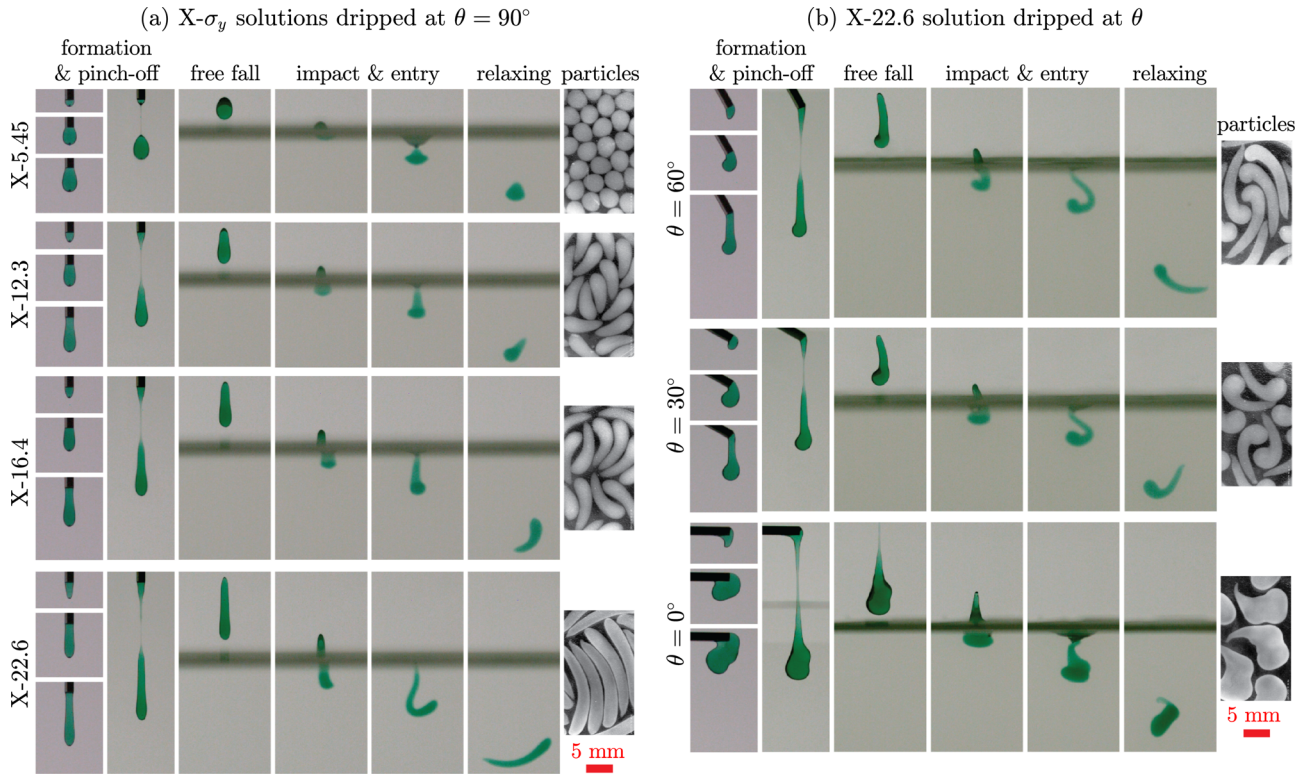

Fig. 5 Using xanthan gum to impart a yield stress. Different stages of particle formation from (a) X-σ_y solutions dripped from a 14G nozzle positioned at $\theta = 90^\circ$ and (b) X-22.6 solution dripped from a nozzle angled at $\theta = 60^\circ$, $\theta = 30^\circ$, or $\theta = 0^\circ$ into a 2 wt% $CaCl_2$ bath. The red scale bars are 5 mm for all images and the corresponding videos are provided in Movies S3 and S4 (ESI†). The image contrast of the X-σ_y particles has been enhanced to increase the visibility of the transparent particles.

Open Access Article. Published on 31 August 2022. Downloaded on 10/18/2025 7:44:19 PM.
This article is licensed under a Creative Commons Attribution-NonCommercial 3.0 Unported Licence.

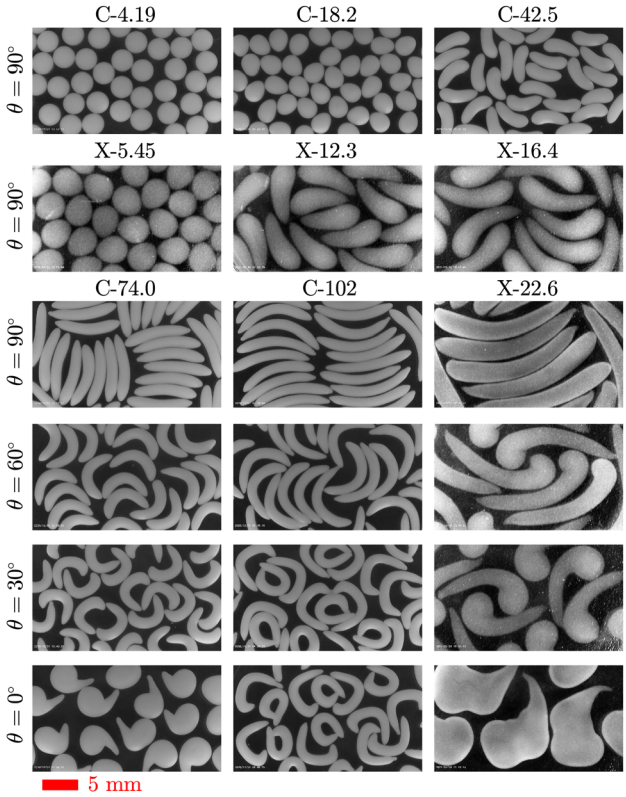

Fig. 6 Images of all particles produced by dripping C-σ_y or X-σ_y solutions from a 14G nozzle positioned at θ = 90°, θ = 60°, θ = 30°, or θ = 0° into a 2 wt% $CaCl_2$ bath. The red scale bar is 5 mm for all images. The image contrast has been enhanced for X-σ_y particles to increase their visibility.

crosslinking reaction is complete. The final shape of X-σ_y particles at their equilibrium swollen state are shown in the last column of Fig. 5(a).

The effect of nozzle orientation on the shape of alginate particles made from X-22.6 solution is demonstrated in Fig. 5(b). Droplets with a rounded tip and a large tail (tadpole-shape) are generated for θ = 60° and are further buckled after bath entry. By decreasing the angle to θ = 30°, the droplet tip becomes larger and the tail length decreases. At θ = 0°, the X-22.6 solution's behavior is similar to the C-74.0 solution. The droplet tip attaches to the nozzle wall and the droplet coils up at the nozzle tip. As the fluid is extruded, the weight of the droplet increases and it detaches from the nozzle wall to finally pinch off. The impact, entry, relaxation, and gelation stages are similar to producing particles from C-74.0 and C-102 solutions using a tilted nozzle tip. The final shape of particles are depicted in the last column of Fig. 5(b). It can be seen from Fig. 5 that the sizes of X-σ_y particles are considerably larger than the initial droplets. This suggests that, unlike C-σ_y particles, X-σ_y particles swell in the bath during crosslinking and their water uptake continue increasing after transferring them into DI water. In addition, X-σ_y particles are larger and more transparent compared to the opaque C-σ_y particles (Fig. 6) and their transparency increases over time in DI water. Note that the image contrast of X-σ_y particles has been enhanced in Fig. 5 and 6 to increase the visibility of the transparent particles. As mentioned earlier, the shrinkage behavior of C-σ_y particles is due to alginate crosslinking and Carbomer microgel deswelling and precipitating in the presence of Ca^{2+} ions. Carbomer precipitation also gives rise to the white nontransparent appearance of the C-σ_y particles. However, X-σ_y particles become more transparent as their water uptake increases.

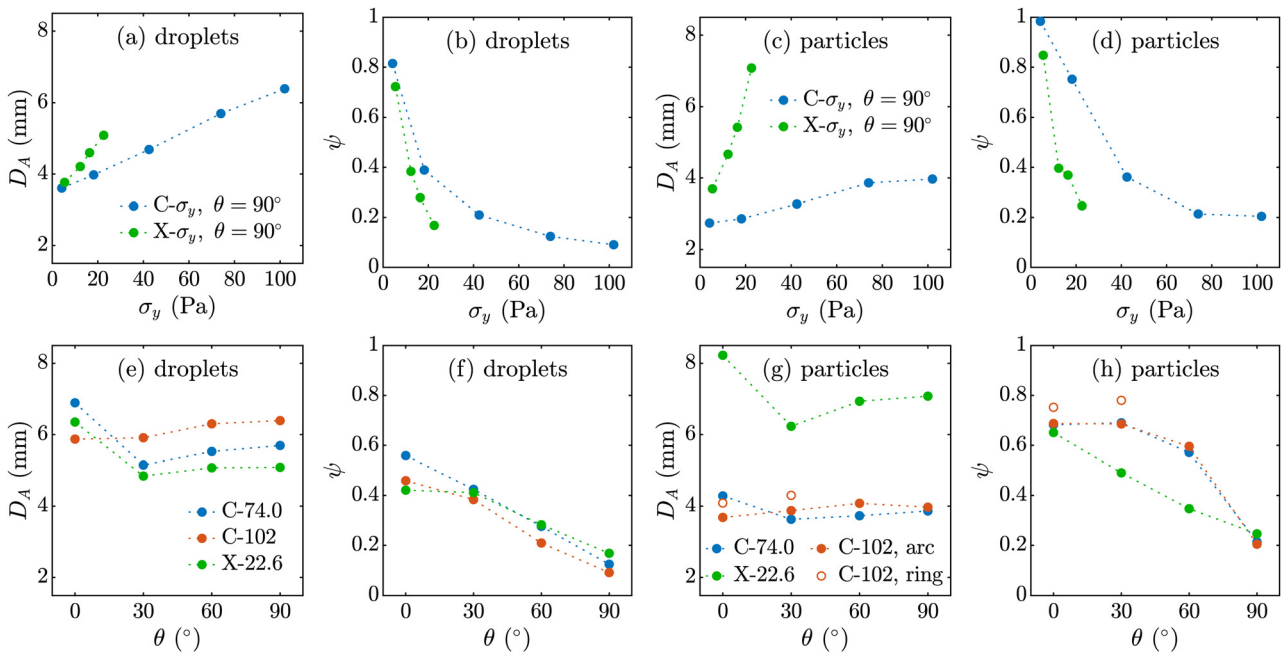

Fig. 7 Projected area diameter, D_A, and Feret ratio, ψ, *versus* (a), (b) σ_y for droplets, (c), (d) σ_y for particles, (e), (f) θ for droplets, and (g), (h) θ for particles. Each data point is the average of 3 trials and the error bars (not shown) are smaller than the marker size. Dotted lines are used as a guide for the eyes.

 This journal is © The Royal Society of Chemistry 2022

Open Access Article. Published on 31 August 2022. Downloaded on 10/18/2025 7:44:19 PM.
This article is licensed under a Creative Commons Attribution-NonCommercial 3.0 Unported Licence.

Fig. 7 depicts the analysis of the size and shape of the viscoplastic droplets and crosslinked particles in their equilibrium swollen state. We use two parameters for our analysis: projected area diameter, D_A, and the Feret ratio, ψ, defined as the ratio of minimum to maximum Feret diameter. Fig. 7(a)–(d) shows that D_A increases with σ_y for both droplets and particles. However, the Feret aspect ratio, ψ, decreases from ≈ 1 for the semi-spherical C-4.19 particles to ≈ 0.2 for C-102 particles. Thus, as σ_y increases, the droplets and particles become larger and more prolate. Fig. 7(e) and (h) show that D_A does not change significantly with θ for the droplets and particles (except that the snail-shell shapes produced at $\theta = 0^\circ$ from C-74.0 and X-22.6 solutions have a larger D_A). In addition, ψ, which in this case is a measure of degree of buckling, decreases with θ for both droplets and particles, with the highest value for the ring-shaped particles. An interesting observation in this figure is the size of swollen particles compared to the uncrosslinked droplets which we discussed qualitatively in the previous sections. C-σ_y particles shrink in size after the crosslinking reaction is complete, while X-σ_y particles swell. We found that the degree of shrinkage and swelling increases with σ_y for C-σ_y and X-σ_y particles, respectively (see Fig. S2, ESI†).

Our experiments did not show a substantial change in shape and size of the alginate particles by increasing the $CaCl_2$ bath concentration from 2 to 10 and 20 wt% (Fig. S3, ESI†), consistent with previous work on the effect of $CaCl_2$ concentration on the morphology of tail-shaped alginate particles.[40]

4 Conclusions

We report a new method that leverages the flow features of viscoplastic fluids to produce shape-engineered alginate particles. A viscoplastic solution composed of sodium alginate and a yield-stress material (either Carbomer or xanthan gum) is dripped into a $CaCl_2$ gelatin bath, where the droplet is subsequently deformed and crosslinked. We find that the morphology of viscoplastic droplets and alginate particles is significantly affected by the yield stress of the solutions, σ_y, nozzle tip orientation with respect to the horizontal direction, θ, and type of the yield-stress material. We explain our observations in terms of (i) a scaling analysis of the forces exerted on the droplet at different stages of particle production, (ii) a competition between the time scales of the viscoplastic fluid relaxation and the crosslinking reaction in the gelation bath, and (iii) the physico-chemical properties of the yield-stress material. We demonstrate that this method can produce uniform mm-sized alginate particles with a variety of shapes resembling spheres, eggs, rice grains, arcs, rings, snail shells, tears, and tadpoles. Our technique will find application in pharmaceutical, food, and cosmetic industries that can benefit from non-spherical particles. Future studies will focus on: (i) producing a wider range of morphologies, (ii) exploring how other parameters, such as impact velocity, alter the shape of particles, and (iii) optimizing our technique to produce non-spherical micron-sized alginate particles.

Conflicts of interest

There are no conflicts to declare.

Acknowledgements

We acknowledge support from the Robert T. Haslam (1911) Chair to PSD. Financial support for AZN was provided by the Pharmaceutical Innovation Programme Singapore (grant number A19B3a0012). We also thank Professor Gareth McKinley's lab at MIT for providing the high-speed camera used in our experiments.

Notes and references

1 K. Y. Lee and D. J. Mooney, *Chem. Rev.*, 2001, **101**, 1869–1880.
2 A. C. Daly, L. Riley, T. Segura and J. A. Burdick, *Nat. Rev. Mater.*, 2020, **5**, 20–43.
3 L. Van Gheluwe, I. Chourpa, C. Gaigne and E. Munnier, *Polymers*, 2021, **13**, 1285.
4 D. Li, Z. Wei and C. Xue, *Compr. Rev. Food Sci. Food Saf.*, 2021, **20**, 5345–5369.
5 R. Song, S. Cho, S. Shin, H. Kim and J. Lee, *Nanoscale Adv.*, 2021, **3**, 3395–3416.
6 J. Li and D. J. Mooney, *Nat. Rev. Mater.*, 2016, **1**, 16071.
7 T. G. Barclay, C. M. Day, N. Petrovsky and S. Garg, *Carbohydr. Polym.*, 2019, **221**, 94–112.
8 L.-H. Chen, L.-C. Cheng and P. S. Doyle, *Adv. Sci.*, 2020, **7**, 2001677.
9 W.-H. Tan and S. Takeuchi, *Adv. Mater.*, 2007, **19**, 2696–2701.
10 S. Ungphaiboon, D. Attia, G. Gomez d'Ayala, P. Sansongsak, F. Cellesi and N. Tirelli, *Soft Matter*, 2010, **6**, 4070–4083.
11 Y.-C. Lu, W. Song, D. An, B. J. Kim, R. Schwartz, M. Wu and M. Ma, *J. Mater. Chem. B*, 2015, **3**, 353–360.
12 A. U. Ernst, L.-H. Wang and M. Ma, *Adv. Healthcare Mater.*, 2019, **8**, 1900423.
13 F. Yanagawa, S. Sugiura and T. Kanamori, *Regener. Ther.*, 2016, **3**, 45–57.
14 H. Zhang, Y. Cong, A. R. Osi, Y. Zhou, F. Huang, R. P. Zaccaria, J. Chen, R. Wang and J. Fu, *Adv. Funct. Mater.*, 2020, **30**, 1910573.
15 G. C. Le Goff, R. L. Srinivas, W. A. Hill and P. S. Doyle, *Eur. Polym. J.*, 2015, **72**, 386–412.
16 S. Masoomi Dezfooli, N. Gutierrez-Maddox, A. Alfaro and A. Seyfoddin, *Rev. Aquac.*, 2019, **11**, 631–660.
17 D. Gokhale, I. Chen and P. S. Doyle, *ACS Appl. Polym. Mater.*, 2022, **4**, 746–754.
18 A. D. Augst, H. J. Kong and D. J. Mooney, *Macromol. Biosci.*, 2006, **6**, 623–633.
19 K. Y. Lee and D. J. Mooney, *Prog. Polym. Sci.*, 2012, **37**, 106–126.
20 B.-B. Lee, P. Ravindra and E.-S. Chan, *Chem. Eng. Technol.*, 2013, **36**, 1627–1642.

Open Access Article. Published on 31 August 2022. Downloaded on 10/18/2025 7:44:19 PM.
This article is licensed under a Creative Commons Attribution-NonCommercial 3.0 Unported Licence.

21 J.-Y. Leong, W.-H. Lam, K.-W. Ho, W.-P. Voo, M. F.-X. Lee, H.-P. Lim, S.-L. Lim, B.-T. Tey, D. Poncelet and E.-S. Chan, *Particuology*, 2016, **24**, 44–60.
22 S. H. Ching, N. Bansal and B. Bhandari, *Crit. Rev. Food Sci. Nutr.*, 2017, **57**, 1133–1152.
23 T. I. Klokk and J. E. Melvik, *J. Microencapsulation*, 2002, **19**, 415–424.
24 K.-S. Huang, C.-H. Yang, Y.-S. Lin, C.-Y. Wang, K. Lu, Y.-F. Chang and Y.-L. Wang, Electrostatic droplets assisted synthesis of alginate microcapsules, *Drug Delivery Transl. Res.*, 2011, **1**, 289–298.
25 Y. Zhou, S. Kajiyama, H. Masuhara, Y. Hosokawa, T. Kaji and K. Fukui, *J. Biomed. Sci. Eng.*, 2009, **2**, 287–293.
26 B. B. Paulo, F. d M. Ramos and A. S. Prata, *J. Food Process Eng.*, 2017, **40**, e12591.
27 H. B. Eral, E. R. Safai, B. Keshavarz, J. J. Kim, J. Lee and P. S. Doyle, *Langmuir*, 2016, **32**, 7198–7209.
28 K. Maeda, H. Onoe, M. Takinoue and S. Takeuchi, *Adv. Mater.*, 2012, **24**, 1340–1346.
29 D. Poncelet, V. Babak, C. Dulieu and A. Picot, *Colloids Surf., A*, 1999, **155**, 171–176.
30 D. Dendukuri and P. S. Doyle, *Adv. Mater.*, 2009, **21**, 4071–4086.
31 H. Zhang, E. Tumarkin, R. Peerani, Z. Nie, R. M. A. Sullan, G. C. Walker and E. Kumacheva, *J. Am. Chem. Soc.*, 2006, **128**, 12205–12210.
32 L. Mazutis, R. Vasiliauskas and D. A. Weitz, *Macromol. Biosci.*, 2015, **15**, 1641–1646.
33 Y. Liu, N. Tottori and T. Nisisako, *Sens. Actuators, B*, 2019, **283**, 802–809.
34 D. An, A. Warning, K. G. Yancey, C.-T. Chang, V. R. Kern, A. K. Datta, P. H. Steen, D. Luo and M. Ma, *Nat. Commun.*, 2016, **7**, 12401.
35 D. K. Hwang, D. Dendukuri and P. S. Doyle, *Lab Chip*, 2008, **8**, 1640–1647.
36 Y. Hu, Q. Wang, J. Wang, J. Zhu, H. Wang and Y. Yang, *Biomicrofluidics*, 2012, **6**, 026502.
37 J. A. Champion, Y. K. Katare and S. Mitragotri, *J. Controlled Release*, 2007, **121**, 3–9.
38 N. Abbasi, M. Navi, J. K. Nunes and S. S. H. Tsai, *Soft Matter*, 2019, **15**, 3301–3306.
39 Y. Geng, P. Dalhaimer, S. Cai, R. Tsai, M. Tewari, T. Minko and D. E. Discher, *Nat. Nanotechnol.*, 2007, **2**, 249–255.
40 Y.-S. Lin, C.-H. Yang, Y.-Y. Hsu and C.-L. Hsieh, *Electrophoresis*, 2013, **34**, 425–431.
41 L. Cai, F. Bian, H. Chen, J. Guo, Y. Wang and Y. Zhao, *Chem*, 2021, **7**, 93–136.
42 X. Zhu, C. Vo, M. Taylor and B. R. Smith, *Mater. Horiz.*, 2019, **6**, 1094–1121.
43 Y. Hu, G. Azadi and A. M. Ardekani, *Carbohydr. Polym.*, 2015, **120**, 38–45.
44 T. Dang and S. Joo, *Colloids Surf., B*, 2013, **102**, 766–771.
45 M. Jeyhani, S. Y. Mak, S. Sammut, H. C. Shum, D. K. Hwang and S. S. H. Tsai, *ChemPhysChem*, 2018, **19**, 2113–2118.
46 K. Yoshida and H. Onoe, *Sci. Rep.*, 2017, **7**, 45987.
47 L. Z. Guan, M. C. Gutiérrez, L. Yuste, F. Rojo, M. L. Ferrer and F. del Monte, *Carbon*, 2019, **147**, 408–418.
48 N. J. Balmforth, I. A. Frigaard and G. Ovarlez, *Annu. Rev. Fluid Mech.*, 2014, **46**, 121–146.
49 A. Z. Nelson and R. H. Ewoldt, *Soft Matter*, 2017, **13**, 7578–7594.
50 D. Bonn, M. M. Denn, L. Berthier, T. Divoux and S. Manneville, *Rev. Mod. Phys.*, 2017, **89**, 035005.
51 C. H. Lee, V. Moturi and Y. Lee, *J. Controlled Release*, 2009, **136**, 88–98.
52 A. K. Grosskopf, R. L. Truby, H. Kim, A. Perazzo, J. A. Lewis and H. A. Stone, *ACS Appl. Mater. Interfaces*, 2018, **10**, 23353–23361.
53 B. M. Rauzan, A. Z. Nelson, S. E. Lehman, R. H. Ewoldt and R. G. Nuzzo, *Adv. Funct. Mater.*, 2018, **28**, 1707032.
54 A. Z. Nelson, B. Kundukad, W. K. Wong, S. A. Khan and P. S. Doyle, *Proc. Natl. Acad. Sci. U. S. A.*, 2020, **117**, 5671–5679.
55 A. Z. Nelson, J. Xie, S. A. Khan and P. S. Doyle, *Adv. Mater. Technol.*, 2021, **6**, 2001245.
56 P. Coussot and F. Gaulard, *Phys. Rev. E: Stat., Nonlinear, Soft Matter Phys.*, 2005, **72**, 031409.
57 G. German and V. Bertola, *J. Non-Newtonian Fluid Mech.*, 2010, **165**, 825–828.
58 G. German and V. Bertola, *Phys. Fluids*, 2010, **22**, 033101.
59 A. Geffrault, H. Bessaies-Bey, N. Roussel and P. Coussot, *J. Rheol.*, 2021, **65**, 887–901.
60 J. Boujlel and P. Coussot, *Soft Matter*, 2013, **9**, 5898–5908.
61 C.-E. Brunchi, M. Bercea, S. Morariu and M. Dascalu, *J. Polym. Res.*, 2016, **23**, 123.
62 P. Coussot, *Rheol. Acta*, 2018, **57**, 1–14.
63 M. Jalaal, D. Kemper and D. Lohse, *J. Fluid Mech.*, 2019, **864**, 596–613.
64 W. Xia, C. Wang, Y. Wei, J. Li, Y. Li and L. Yang, *Exp. Fluids*, 2020, **61**, 57.
65 J.-S. Hong and J. J. Cooper-White, *Korea Aust. Rheol. J.*, 2009, **21**, 269–280.
66 H. Kim, *Korean J. Chem. Eng.*, 1990, **7**, 1–6.
67 T. Braschler, A. Valero, L. Colella, K. Pataky, J. Brugger and P. Renaud, *Anal. Chem.*, 2011, **83**, 2234–2242.
68 A. L. Huang, S. V. Desai and R. M. Wellek, *J. Chem. Eng. Data*, 1969, **14**, 356–359.
69 K. T. Campbell, K. Wysoczynski, D. J. Hadley and E. A. Silva, *ACS Biomater. Sci. Eng.*, 2020, **6**, 308–319.
70 Z. Jaworski, T. Spychaj, A. Story and G. Story, *Rev. Chem. Eng.*, 2021, 000010151520200016.
71 A. Nowbahar, A. O'Connor, V. Mansard, P. Spicer and T. M. Squires, *Phys. Rev. Fluids*, 2019, **4**, 061301.
72 T. L. Corporation, *Dispersion Techniques for Carbopol Polymers, Technical Data Sheet TDS-103, The Lubrizol Corporation*, Wickliffe, OH, USA, 2007.
73 N. J. Balmforth and I. J. Hewitt, *J. Non-Newtonian Fluid Mech.*, 2013, **193**, 28–42.
74 K.-W. Song, Y.-S. Kim and G.-S. Chang, *Fibers Polym.*, 2006, **7**, 129–138.
75 A. Z. Nelson, R. E. Bras, J. Liu and R. H. Ewoldt, *J. Rheol.*, 2018, **62**, 357–369.

 This journal is © The Royal Society of Chemistry 2022